JOURNAL OF SPACECRAFT AND ROCKETS
Vol. 45, No. 6, November–December 2008

Stage-Separation Aerodynamics of Two-Stage Space Transport Systems Part 1: Steady-State Simulations

Mochammad A. Moelyadi,* Christian Breitsamter,† and Boris Laschka‡
Technische Universität München, 85747 Garching, Germany

DOI: 10.2514/1.34828

This paper presents steady-state simulations of two-stage space transport systems during separation. The stage separation is simulated in quasi-steady-state flow so that there is no effect of a downwash due to the orbital-stage motion to be considered. The computational model of an orbital stage is set at various positions relative to a carrier stage. The simulations of stage separation considering time-dependent flow will be presented in a separate paper. For the steady-state simulation, two carrier-stage models are used: namely, a flat plate for simplifying interference effects and a fully detailed vehicle (elliptical aerodynamic configuration). In both cases, the orbital stage consists of a detailed configuration (elliptical aerodynamic configuration orbital stage). The steady-flow solutions are obtained by solving the three-dimensional Euler equations using the explicit finite volume shock-capturing method with the modified advection upstream splitting method approach for convective flux evaluation. The simulations are performed on structured multiblock grids with elliptic grid smoothing based on the Poisson equations. Flowfield patterns demonstrating strong interference effects due to incident and reflected shock waves and expansion regions as well as corresponding surface pressure distribution and aerodynamic forces and moments of carrier and orbital stages are analyzed. From the solutions for both configurations, good agreement is found comparing numerical and corresponding experimental results.

Nomenclature

C_D	=	total drag coefficient
C_L	=	total lift coefficient
C_M	=	total pitching-moment coefficient
C_p	=	pressure coefficient
$\mathbf{F}, \mathbf{G}, \mathbf{H}$	=	fluxes in curvilinear and dimensionless coordinate system
$\mathbf{h}_{\mathrm{KOS}}$	=	distance from axis $\mathbf{X}_{\mathrm{EOS}}$ to the flat plate or distance from axis $\mathbf{X}_{\mathrm{EOS}}$ to axis $\mathbf{X}_{\mathrm{ELAC}}$
J	=	Jacobi matrix for the coordinate transformation
$\mathbf{L}$	=	reference length of elliptical aerodynamic configuration orbital stage
M_∞	=	freestream Mach number
$\mathbf{P}, \mathbf{Q}, \mathbf{R}$	=	source terms of grid smoothing
$\boldsymbol{p}$	=	static pressure
$\mathbf{Q}$	=	state variables in the curvilinear and dimensionless coordinate system
u, v, w	=	velocity components
$\mathbf{X}, \mathbf{Y}, \mathbf{Z}$	=	axes of the Cartesian coordinate system of the vehicle stage
x, y, z	=	Cartesian coordinates
$\Delta\alpha$	=	relative angle of attack
ξ, η, ζ	=	curvilinear coordinates
ρ	=	density

I. Introduction

IN THE globalization era, the growing demands on new space transportation systems such as unmanned space vehicles and future-generation reusable launch vehicles have pulled research activities in many hypersonic technological areas in many institutions all over the world [1–3]. In the United States, NASA has put the second-generation reusable launch vehicles as a major program of the Integrated Space Transportation Plan, with $4.8 billion spent to run this program covering the period 2001–2006 [4]. In Europe, several system studies were conducted since the 1990s to investigate possible concepts for a European reusable launch vehicles. Some of the national programs (e.g., SAENGER, STAR-H, and TARANIS) investigate the concepts of two-stage-to-orbit (TSTO) systems instead of single-stage-to-orbit (SSTO) vehicles [1]. A similar two-stage-to-orbit concept program is also being performed in Japan by the institution of Japan Aerospace Exploration Agency. This institution has conducted the High-Speed Flight Demonstrator project as the latest in a series of flight experiments in a research program for reusable space transportation systems [5].

Efforts to develop such hypersonic transportation systems have been performed in Europe with substantial advancements in lightweight high-temperature structural materials, thermal protection systems, propulsion systems, etc. Particularly, in Germany, intensive efforts dealing with the key technologies for a two-stage space transportation system have been supported by three research centers of the Sonderforschungsbereich (SFB): namely, SFB 253 (RWTH Aachen), SFB 255 (Technische Universität München), and SFB 259 (University of Stuttgart). At the Technische Universität München, the research efforts have been focused on transatmospheric flight systems, including fundamentals of aerothermodynamics, power-plants, and flight mechanics [6]. The detail concept of a TSTO vehicle deals with a delta-winged first stage powered by airbreathing engines and a rocket-propelled upper stage (see Fig. 1). The concept was initiated by the idea of Sänger, as noted in [6], that the upper and lower stages are designed as high lift over drag vehicles [7]. Such a space vehicle has a flight mission consisting of three phases, including pull-up, separation process, and standalone phases. In the pull-up phase, the orbital stage is mounted on the back of the carrier aircraft. It is launched horizontally to reach the speed flight of Mach about 6.8 at altitude of 35 km. In this position, the orbital stage is released and the separation process (as the second phase) starts. The orbital stage separates from the carrier stage until the standalone-flight phase takes place, and so no interaction occurs between the stages. Among the phases of the ascent flight mission, the separation

Received 27 September 2007; revision received 13 June 2008; accepted for publication 7 July 2008.

*Research Engineer, Institute of Aerodynamics; moelyadi1968@hotmail.com.
†Chief Scientist, Institute of Aerodynamics; Christian.Breitsamter@aer.mw.tum.de. Associate Fellow AIAA.
‡Professor Emeritus, Institute of Aerodynamics; Laschka@aer.mw.tum.de. Honorary Fellow AIAA.

maneuver will be the most critical one for the vehicle system. In such a phase, very high dynamic pressures are subject to the space vehicle system. Under these conditions, aerodynamic interferences occur between the stages: namely, complex interactions of incident and reflected shock waves and expansion waves with each other as well as with boundary layers. Furthermore, the separation process influences the position and intensity of the shock waves and the points of interaction of the reflected shock waves that provide strong unsteady airloads on both stages. This may have an impact on the stability of the vehicle during the separation maneuver and causes a hazard during the space vehicle operation.

Our stage-separation aerodynamics study of two-stage transport systems will be separated in two parts. This paper, as part 1, presents the steady-state simulation of two-stage space transport system during separation based on computational fluid mechanics. Part 2, which considers the simulation of the stage separation with time-dependent flow, will be presented in a separate paper. In the first study, the stage separation is simulated in quasi-steady-state flow by setting a computational model of an orbital stage at various positions relative to a carrier stage. The simulations do not consider the effects of a downwash due to the orbital-stage motion. For obtaining steady-flow solutions, the simulations solve three-dimensional unsteady Euler equations to reduce computational time and cost. The study is carried out for two different carrier-stage models: namely, a flat plate and a fully detailed vehicle [elliptical aerodynamic configuration (ELAC)]. In both cases, the orbital stage consists of a detailed configuration [ELAC orbital stage (EOS)]. At the beginning of the simulations, the use of a combination of a flat plate and an EOS model is to simplify interference effects and to obtain fast and reasonable numerical solutions. The results of steady-flow calculations for both configurations are compared with the corresponding experimental data from tests at the T-313 supersonic wind tunnel at the Institute of Theoretical and Applied Mechanics [8]. To know the effects of quasi-steady stage separation on flow features and aerodynamic forces and moments of the space vehicle system, important parameters of the stage separation (such as orbital angle of attack and separation distance as well as Mach number) are analyzed.

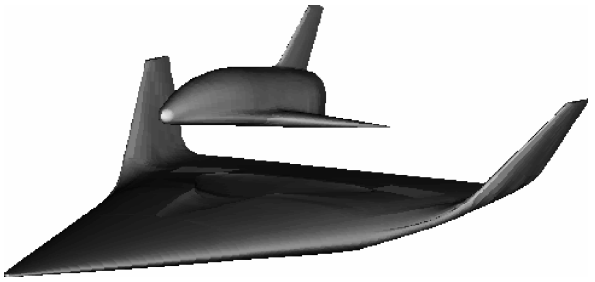

Fig. 1 Two-stage space transport vehicle (EOS–ELAC).

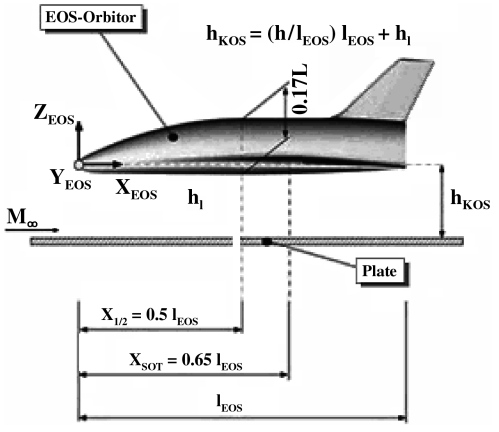

Fig. 2 Basic geometry of the EOS and flat plate.

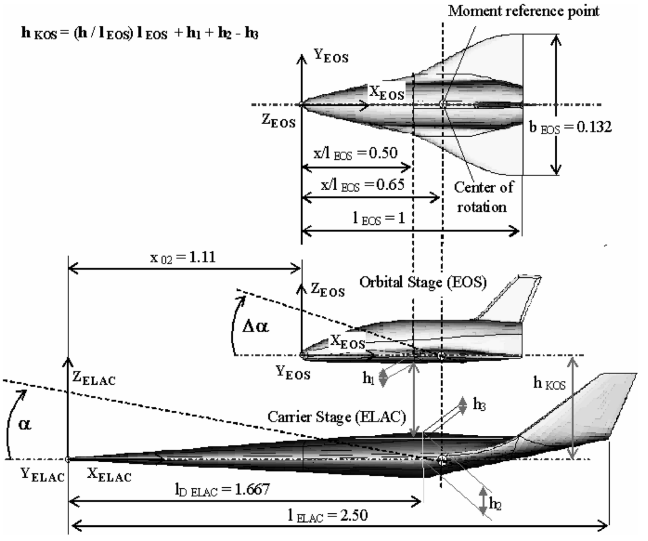

Fig. 3 Configuration and geometric reference values of EOS and ELAC space transport systems.

II. Geometry, Mesh Generation, and Flow Solver

For computational simulations of the stage separation of a TSTO model, the proper geometry, high-quality meshes, and a robust and accurate numerical method are required to obtain reasonable

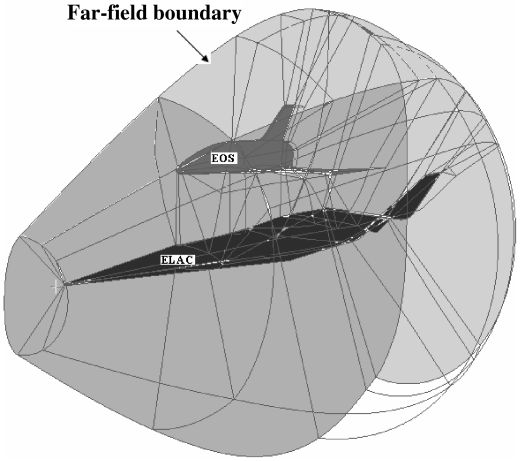

Fig. 4 Computational domain and topology blocks for the ELAC–EOS configuration.

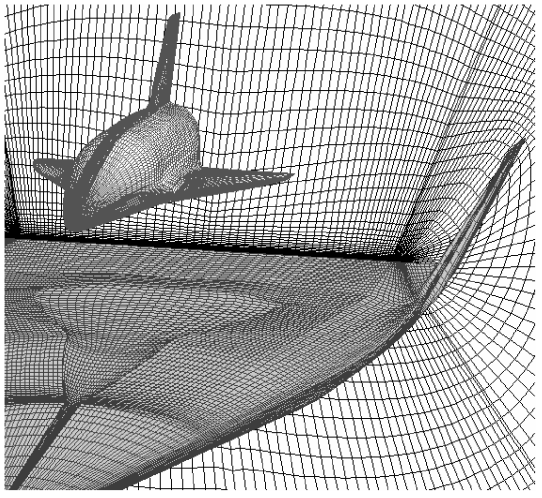

Fig. 5 Smoothed grids of the ELAC–EOS configuration.

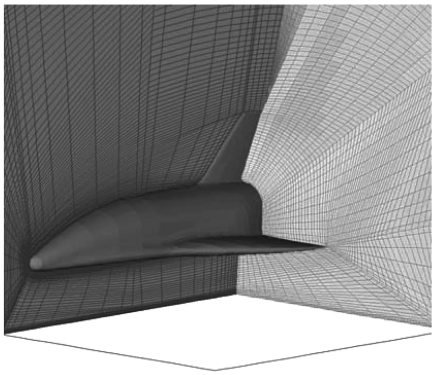

a) Low smoothing

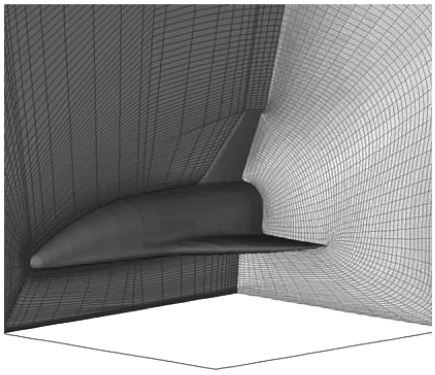

b) Adequate smoothing

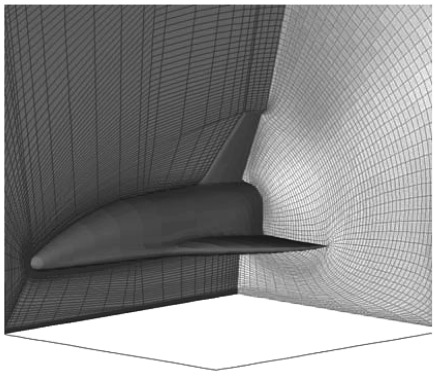

c) High smoothing

Fig. 6 Effect of grid smoothing on grid quality.

solutions of the flowfield. The flowfield in the region between the stages is dominated by aerodynamic interferences such as unsteady flow, shock waves, and expansion waves and is also accompanied by viscous flow effects. All of these phenomena have nonlinear behavior that may cause difficulties in the simulations. A detailed description of the numerical simulation for the TSTO stage separation is given as follows.

A. Geometry of the TSTO Vehicle System

As shown in Fig. 1, the space transportation system consists of two stages: namely, the carrier stage and the orbital stage. The simplified carrier stage using a flat surface and the geometry of the EOS orbital stage are depicted in Fig. 2.

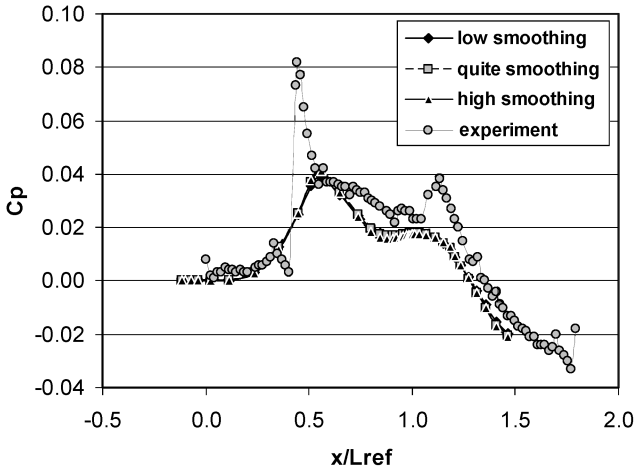

Fig. 7 Pressure coefficient distribution on the symmetry line of the flat plate ($y = 0$) at $M_\infty = 4.04$, $\Delta\alpha = 0.0\,\text{deg}$, and $h/l_{\text{EOS}} = 0.150$.

Moreover, the full geometry of the ELAC carrier stage has a length of 2.5 of the EOS orbital stage, as depicted in Fig. 3. Such a carrier stage has a sharp nose with a body designed as a slender blended wing–body shape like a wave rider with swept wing tips. In the middle part of the upper surface of the carrier stage, a large cavity is made to place the orbital stage. In addition, the lower surface of the carrier stage was designed as a ramp, due to the placement of airbreathing propulsion. Concerning the EOS orbital stage, it has a blunt nose and its body was designed as a nearly circular cross section (as with the space shuttle) and was equipped with a delta wing and vertical stabilizer. For the EOS–flat-plate model, the parameter $\mathbf{h}_{\text{KOS}}$ refers to the distance from axis $\mathbf{X}_{\text{EOS}}$ to the flat plate, and $\boldsymbol{l}$EOS is the body length of EOS. In addition, the distance of $\mathbf{h}_{\text{KOS}}$ for the ELAC–EOS model is between the axes $\mathbf{X}_{\text{ELAC}}$ and $\mathbf{X}_{\text{EOS}}$ of the stages. The parameter $\mathbf{h}_{\text{KOS}}$ of each model is measured with a mathematical relation stated in each figure. The parameter of relative distance is given by h/l_{EOS}. The angle of attack α is measured based on the X axis of the ELAC model, and the relative angle of attack $\Delta\alpha$ of the EOS model is calculated based on the X axis of the flat plate or ELAC model.

B. Mesh Generation

The procedure for generating the grids for steady-flow calculations includes block topology generation, initial mesh generation, and treatment for mesh smoothing. Initially, the CFD domain is defined starting from the vehicle surface to a far-field boundary. A multiblock segmentation of the computational domain of interest is then made using ICEMCFD HEXA by defining a block topology [9]. Such a block topology can then be refined into smaller blocks to fit with the geometry by splitting and merging blocks, as well as using a special tool called O-grid. The computational domain of the half-configuration of the detailed EOS and ELAC is shown in Fig. 4.

Once the overall blocks are prepared, the points for each block are distributed along the edges of the block. It is necessary to concentrate a major number of points in critical regions such as on the leading- and trailing-edge sections of the main wing and the vertical tail of the EOS and the wing tip of the ELAC and in the wake region behind the base of both vehicles. The point distribution also becomes denser when the points are approaching the body surface. The internal

Table 1 Effect of smoothed grids on aerodynamic characteristics at $M_\infty = 4.04$, $\Delta\alpha = 0.0\,\text{deg}$, and $h/l_{\text{EOS}} = 0.150$

					% difference		
	Low	Adequate	High	Exp.	Low	Adequate	High
Lift coef. C_L	−0.00939	−0.01070	−0.01148	−0.01150	18.3%	7.0%	0.2%
Drag coef. C_D	0.0269	0.0262	0.0264	0.0294	8.5%	10.9%	10.2%
Pitching-moment coef. C_M	−0.0107	−0.0109	−0.0110	−0.0041	161.0%	165.9%	168.3%

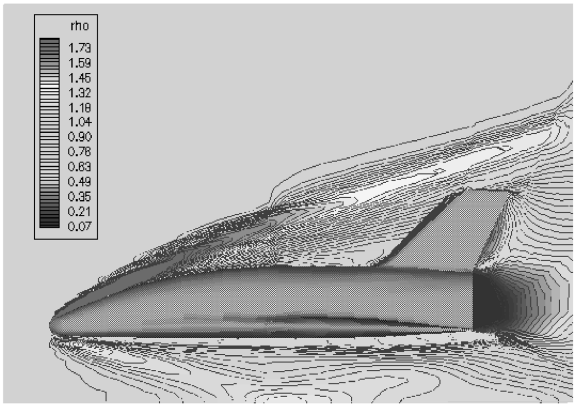

a) Coarse grid

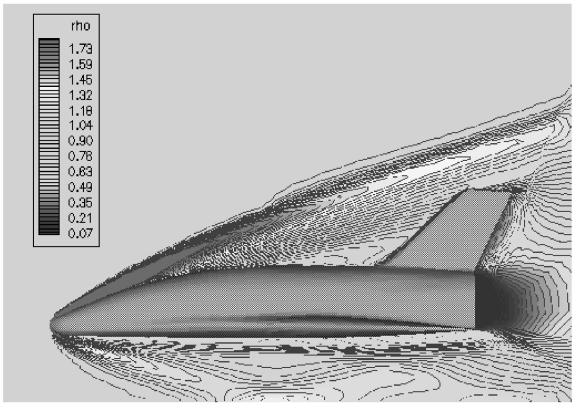

b) Standard grid

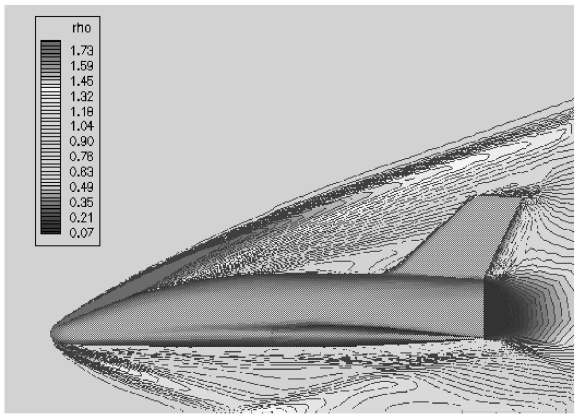

c) Finer grid

Fig. 8 Density contours for different grid densities at $M_\infty = 4.04$, $\Delta\alpha = 0.0\,\text{deg}$, and $h/l_{\text{EOS}} = 0.150$.

points on the face and in the volume of each block are then generated by interpolating the given points, and hence the initial basic structured grids are the result. Subsequently, to have a good smoothness and orthogonality of the grids, a grid-smoothing process is performed by solving a system of Poisson vector equations that is given in [10]. The results of the smoothed grids inside the computational domain and on the surface for the ELAC–EOS model are shown in Fig. 5.

C. Flow Solver

The numerical solution of steady flow is obtained by solving the three-dimensional Euler equations. Using a finite volume approximation, the integral form of the unsteady Euler equations is discretized in computational space and transformed into a nonlinear algebraic vector equation. Such a differential equation system may be expressed in strong conservation form and curvilinear coordinates as

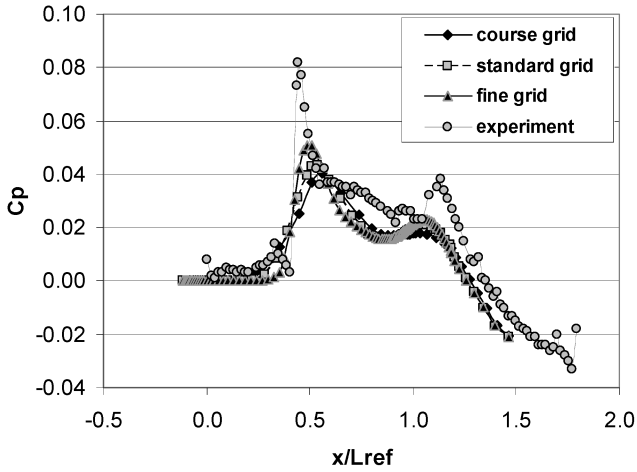

Fig. 9 Pressure coefficient distribution on symmetry line of flat plate for three different grid densities.

$$\frac{\partial Q}{\partial \tau} + \frac{\partial F}{\partial \xi} + \frac{\partial G}{\partial \eta} + \frac{\partial H}{\partial \zeta} = 0 \tag{1}$$

where $\mathbf{Q}$ is the vector of conservative variables ($\mathbf{Q} = J[\,\rho \quad \rho u \quad \rho v \quad \rho w \quad e\,]^T$, where J is the Jacobian transformation), and $\mathbf{F}$, $\mathbf{G}$, and $\mathbf{H}$ are the inviscid conservative fluxes with respect to the ξ, η, and ζ directions, respectively.

The numerical method used to solve Eq. (1) is based on the explicit finite volume shock-capturing method. The time-dependent flow vector is calculated by using the Strang-type of fractional step [11]. The calculation of the numerical fluxes between cells is performed by the modified AUSM (advection upstream splitting method) according to Radespiel and Kroll [12]. This scheme represents a hybrid approach between the van Leer flux-vector splitting scheme and the original AUSM scheme developed by Liou and Steffen [13]. The AUSM scheme is based on the idea to regard the convection and acoustic waves as physically distinct processes and thus define the fluxes as a sum of the convective and pressure terms. In a region with intensive shock waves, the flux-vector splitting method is used to show a good resolution of the shock. In addition, to guarantee high-order accuracy in the spatial domain, the left and right states at the cell interfaces are obtained with the MUSCL approach [14]. The limiter function is chosen to extrapolate the state values and thus provide higher-order fluxes in smooth regions. At discontinuities, the function switches to first-order accuracy to ensure optimal shock-capturing features.

On an impermeable wall, characteristic boundary conditions are applied to evaluate the primitive variables. At the far-field boundary, the flow variables are set to their freestream values for hypersonic inflow conditions, whereas for outflow conditions, the flow variables are extrapolated by employing the solution of the computational domain.

III. Analysis of Computational Results of TSTO Separation Maneuver

A. Numerical Grid Study and Validations

To check the accuracy of the steady-state simulation, the studies on numerical grids including grid smoothing and grid density are carried out for the flat-plate–EOS model. The computational results are then compared with the corresponding experimental data, which are taken from the T-313 supersonic wind tunnel [6]. The experimental test condition is at a freestream Mach number of 4.0, unit Reynolds number of 50.0×10^6, related dynamic pressure of 73.5 kPa, and freestream temperature of 294 K.

For the validation, the model of the EOS orbital stage is positioned at the angle of attack $\Delta\alpha = 0.0$ deg and the distance $h/l_{\text{EOS}} = 0.150$ relative to the flat plate with a freestream Mach number of 4.0. The results of computational grid quality for three different grids obtained by the smoothing process (namely, low, adequate, and high grid

Table 2 Effect of grid density on aerodynamic characteristics $M_\infty = 4.04$, $\Delta\alpha = 0.0$ deg, and $h/l_{\text{EOS}} = 0.150$

					% difference		
	Coarse grid	Standard grid	Finer grid	Exp.	Coarse grid	Standard grid	Finer grid
Lift coef. C_L	−0.0107	−0.01138	−0.0118	−0.0115	7.0%	1.0%	2.6%
Drag coef. C_D	0.0262	0.0273	0.0277	0.0294	10.9%	7.1%	5.8%
Pitching-moment coef. C_M	−0.0109	−0.0104	−0.0106	−0.0041	165.9%	153.7%	158.5%

qualities with the grid errors of 10^{-2}, 10^{-3}, and 3×10^{-4}, respectively) are shown in Figs. 6a–6c. The higher grid quality provides a more accurate lift coefficient compared with the corresponding experimental data, as given in Table 1. However, the drag coefficients are almost not affected by the grid smoothing. Compared with the experimental data, the computed drag gives about 10% error. This is caused by the strength of the shock wave, which is not yet simulated properly due to inadequate grid number and the viscous effects not considered in the flow equation, as exhibited by the pressure distribution on the symmetry line of the flat plate in Fig. 7. Here, the experimental result of pressure distribution is measured on the symmetry line of the flat plate [8].

Increasing the grid number along the EOS body surface provides better capturing in the shock waves, as shown Figs. 8a–8c: namely, the graphs of density contours for three different grid numbers of 113×10^3, 252×10^3, and 493×10^3 grids, respectively. It is also indicated clearly by a graph of pressure distributions along the symmetry line of the flat plate shown in Fig. 9. Two peak pressures generated by the shock waves on the flat plate for the finer grid is the closest to the corresponding experiment result, but the second peak pressure behind the base of the experiment cannot be captured well for all computational cases. Table 2 provides aerodynamic forces and moments for the three different grid numbers and the corresponding

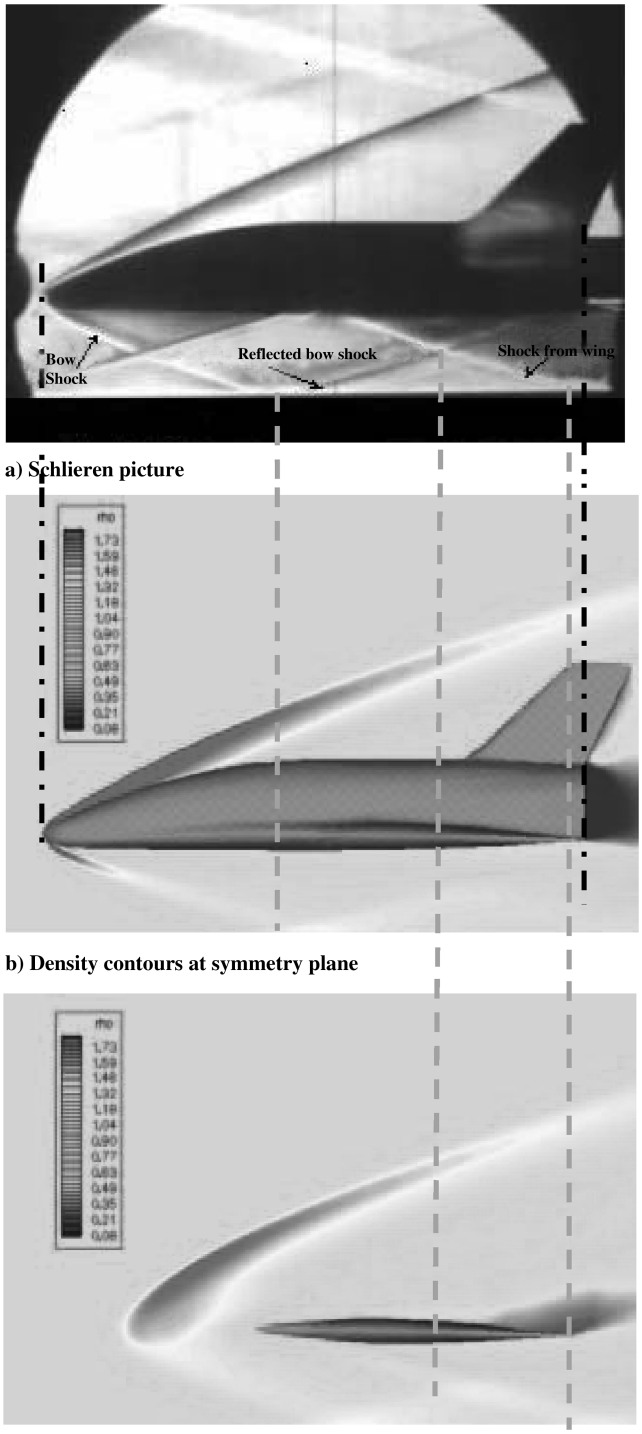

a) Schlieren picture

b) Density contours at symmetry plane

c) Density contours on plane at station y/s = 0.1

Fig. 10 Schlieren picture and density contour for flat-plate–EOS at $M_\infty = 4.0$, $\Delta\alpha = 0.0$ deg, and $h/l_{\text{EOS}} = 0.150$.

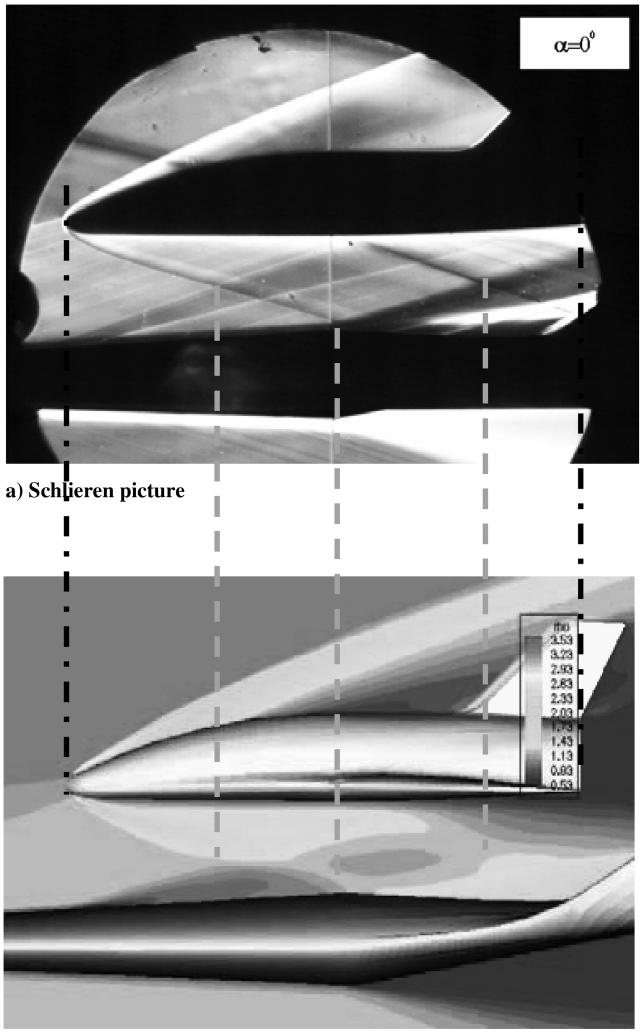

a) Schlieren picture

b) Density contours at symmetry plane

Fig. 11 Schlieren picture and density contour for ELAC–EOS at $M_\infty = 4.0$, $\Delta\alpha = 0.0$ deg, $\alpha = 0.0$ deg, and $h/l_{\text{EOS}} = 0.225$.

Table 3 Aerodynamic characteristics of ELAC–EOS configuration at $M_\infty = 4.0$

	EOS vehicle			ELAC vehicle		
	Comp	Exp	% difference	Comp	Exp	% difference
Lift coef. C_L	0.0292	0.0366	20.2%	−0.0504	−0.0491	2.6%
Drag coef. C_D	0.0293	0.0337	13.1%	0.0133	0.0164	18.9%
Pitching-moment coef. C_M	−0.0073	−0.0072	1.4%	0.0077	0.0089	13.5%

experiment data for reference. The increase of grid density causes the reduction of the discrepancy of lift coefficient from 7 to 1% and that of the drag coefficient from 11 to 6%, compared with the corresponding experimental data. Subsequently, all computation results for flat-plate–EOS configuration are computed using the finer grid.

Concerning the pitching-moment coefficient, the computed results in Tables 1 and 2 exhibit a slight change with increasing the level of grid smoothing and the number of grids. But compared with the corresponding experimental data, they show a great disparity. This is due to the lack of simulating of a shock wave that generated by the leading edge of the flat plate, as shown in Fig. 10. The absence of a shock wave emanating from the leading edge of the flat plate in the simulation is because the flat plate is modeled as an infinite plate. In the experiment, such a shock wave hitting the lower surface of the orbital stage provides an additional load that contributes a less negative pitching-moment coefficient of the orbital stage. The inflection point on the lower surface occurs at about $x/l_{\text{EOS}} = 0.46$ with respect to the nose of the EOS stage that is in the front of the pitching-moment reference of the orbital stage ($x/l_{\text{EOS}} = 0.65$).

Figure 10 shows a comparison between the schlieren picture and the computed density distribution of the flat-plate–EOS configurations The relative density contours are recorded in the symmetry plane and in the plane at a station $y/s = 0.1$. The relative density is stated as a ratio of density at a certain point of the flowfield to the freestream density, ρ/ρ_∞. The simulation can capture in a good accuracy level for the EOS bow shock, reflected bow shock, and shock emanating from the inflection of the wing leading edges, compared with the corresponding experimental result, except the shock wave from the leading edge of the flat plate. In addition, minor differences appear dealing with the positions of shock waves. Compared with the experiment, the location of the computed reflected shock wave and impingement point are slightly rearward. This disparity is also indicated by the static-pressure distribution in Fig. 9. The calculated pressure peaks caused by the impinging bow shock emanating from the blunt nose of the orbital stage and the wing are weaker than with the experimental reference data.

The subsequent validation is performed for the configuration of the ELAC and EOS stages. Figure 11 shows a schlieren picture and relative density contours at $M_\infty = 4.0$, $\alpha = 0.0$ deg, $\Delta\alpha = 0.0$ deg, and $h/l_{\text{EOS}} = 0.225$. The density contours are obtained at the symmetry plane around the stages. Qualitatively, almost all flow features of the experimental result can be captured in the simulation with satisfying accuracy. At this condition, the bow shock wave of ELAC impinges on the bow shock of EOS, close to the EOS nose. The bow shock wave of EOS spreads out downstream around the EOS body, but in the symmetry plane, it can only be seen above and below the EOS surface. A part of the bow shock wave goes to the flowfield above EOS, forming a line with a certain angle φ_u, and the other part goes to the flowfield beneath EOS, forming another line with a certain angle φ_l. The computational results show a slight difference in bow shock angles compared with the experimental result. Subsequently, the latter shock wave hits the middle part of the ELAC surface. Although the flow on the upper surface of the ELAC experiences an expansion through a beginning of the curvature of the ELAC cavity, it forms expansion waves in the flow region between

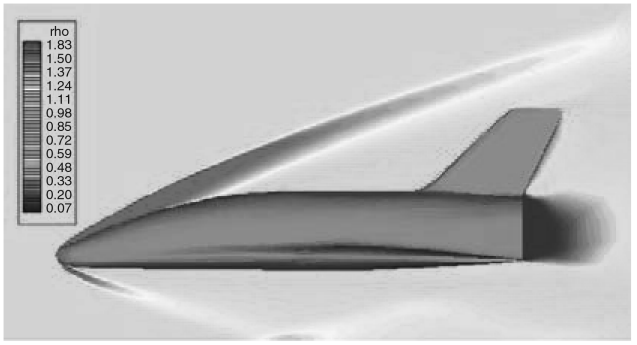

a) h/l$_{\text{EOS}}$ = 0.150, Δα = 0.0 deg

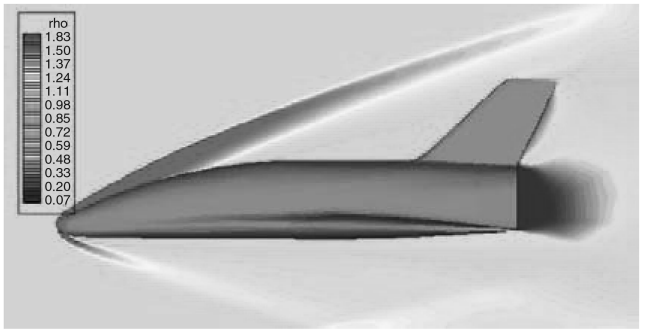

b) h/l$_{\text{EOS}}$ = 0.225, Δα = 0.0 deg

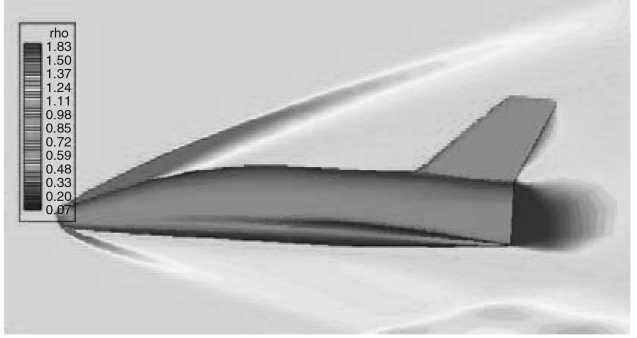

c) M$_\infty$ = 4.0; h/l$_{\text{EOS}}$ = 0.225, Δα = 3.0 deg

Fig. 12 Effects of relative distance and relative angle on flow behavior of the flat-plate–EOS configuration at $M_\infty = 4.0$.

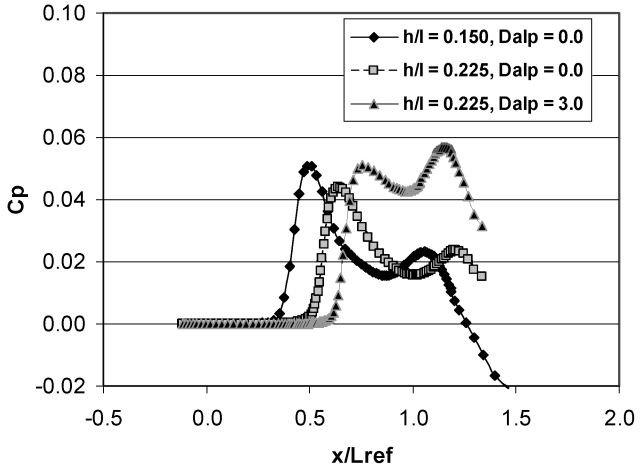

Fig. 13 Pressure coefficient distribution on the symmetry line of a flat plate for three different EOS positions at $M_\infty = 4.0$.

Table 4 Comparison of aerodynamic characteristics for three different EOS positions at $M_\infty = 4.0$

	$h/l_{\text{EOS}} = 0.150$, $\Delta\alpha = 0.0$			$h/l_{\text{EOS}} = 0.225$, $\Delta\alpha = 0.0$			$h/l_{\text{EOS}} = 0.225$, $\Delta\alpha = 3.0$		
	Comp	Exp	% diff	Comp	Exp	% diff	Comp	Exp	% diff
Lift coef. C_L	−0.0118	−0.0115	2.6%	−0.0127	−0.0120	5.8%	0.0263	0.0293	10.2%
Drag coef. C_D	0.0277	0.0294	5.8%	0.0277	0.0299	7.4%	0.0283	0.0304	6.9%
Pitching-moment coef. C_M	−0.0106	−0.0041	158.5%	−0.0084	−0.0059	42.4%	−0.0071	−0.0062	14.5%

the ELAC and EOS, but this phenomena cannot be shown clearly in the simulation. At the ELAC cavity, the flow also exhibits a shock wave, due to the curved surface downstream. This shock wave also spreads out in the same region. Both the expansion and shock waves interact with the extended bow shock of the EOS occurring in the middle flow region between the ELAC and EOS. Downstream, the shock wave continues through the flowfield and hits the rear part of the lower surface of the EOS.

Concerning the aerodynamic characteristics, Table 3 provides the comparison between the computational results and the experimental data of the ELAC and EOS stages. The calculated aerodynamic coefficients for the carrier stage show a better agreement with the experiment results than those of the orbital stage. This is caused by the complex aerodynamic interactions due to shock waves and expansion waves occurring on a larger part of the orbital-stage area than with the carrier stage. Considering the aerodynamic characteristics of the first configuration (flat plate–EOS) in Table 2, the ELAC configuration contributes to a positive lift of the EOS stage and, contrarily, the flat-plate interference results in a negative lift of the EOS stage. The additional drag of the EOS stage of the second configuration is due to the influence of the expansion and shock waves generated at the beginning of the curvature of the ELAC cavity. In addition, the prediction of pitching moment of the ELAC–EOS configuration provided in Table 3 is much better than that of the flat-plate–EOS configuration in Table 2. This is because almost all flow features of the experimental result of the ELAC–EOS configuration, including interactions of incident and reflected shock waves in the gap region between both stages and expansion waves under the lower surface of ELAC, can be captured in the simulation with satisfying accuracy, as shown in Fig. 11.

B. Quasi-Steady Stage Separation: Flat Plate/EOS

As mentioned in the introduction, the stage separation is simulated in quasi-steady-state flow by setting a computational model of an orbital stage at various positions relative to a carrier stage. For the flat-plate–EOS configuration, the effects of the positions of the orbital stage (including relative distance h/l_{EOS} and relative angle of attack $\Delta\alpha$) on the flowfield and aerodynamic performance at freestream Mach number of 4.0 are studied. The influence of the change in relative distance are shown by the density contours in Figs. 12a and 12b. It leads to a shift of the inflection and interaction points of the shock wave to the rear.

As shown in the graph of the static-pressure distribution in Fig. 13, the shock strength at the first inflection point due to the bow shock

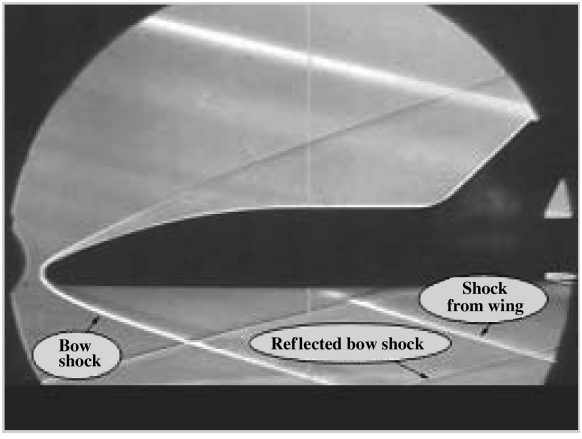

Fig. 14 Schlieren picture for the flat-plate–EOS configuration at $M_\infty = 4.0$, $\Delta\alpha = 0.0$ deg, and $h/l_{\text{EOS}} = 0.225$.

Table 5 Comparison of aerodynamic characteristics for three different Mach number at $h/l_{\text{EOS}} = 0.150$ and $\Delta\alpha = 0$

	$M_\infty = 4.0$	$M_\infty = 6.8$	$M_\infty = 7.9$
Lift coef. C_L	−0.01180	−0.01540	−0.01541
Drag coef. C_D	0.0277	0.0222	0.0213
Pitching-moment coef. C_M	−0.0106	−0.0093	−0.0091

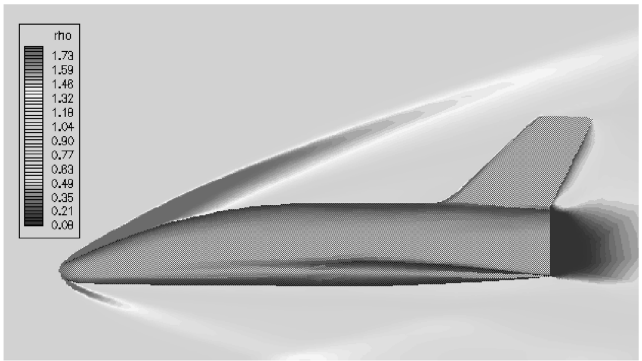

a) $M_\infty = 4.0$

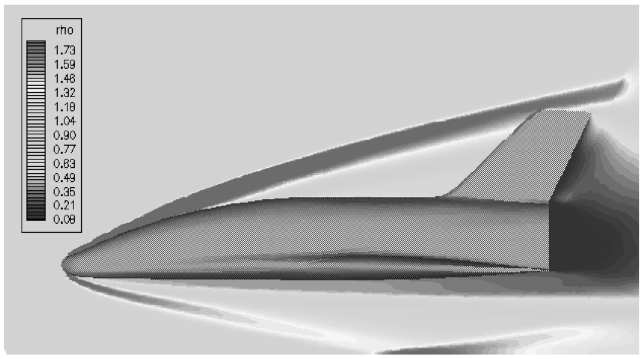

b) $M_\infty = 6.8$

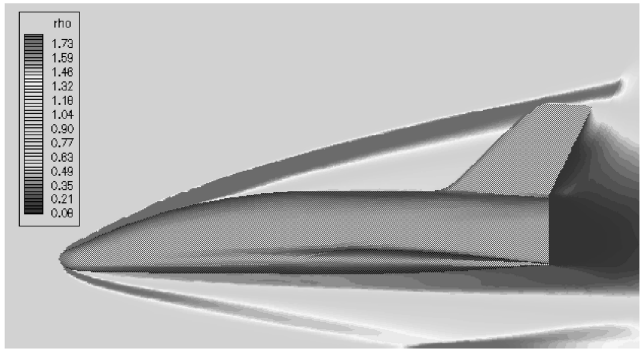

c) $M_\infty = 7.9$

Fig. 15 Effects of freestream Mach number on flow behavior at $h/l_{\text{EOS}} = 0.150$ and $\Delta\alpha = 0.0$ deg.

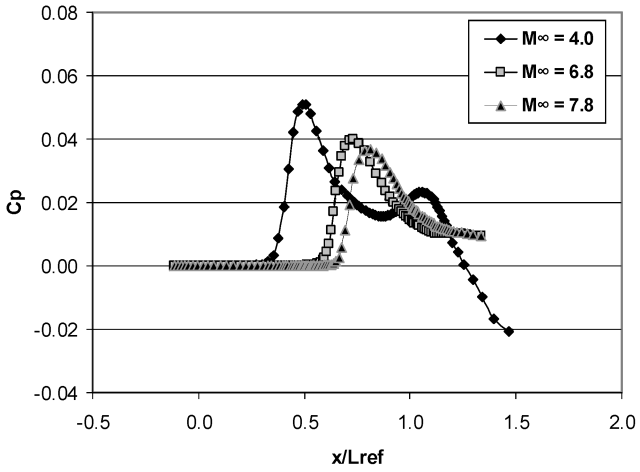

Fig. 16 Pressure coefficient distribution on symmetry line of flat plate for three different Mach numbers at $h/l_{\mathrm{EOS}} = 0.150$ and $\Delta\alpha = 0$.

decreases, but the shock strength at the second inflection point generated by the shock from the wing slightly increases. Concerning the change in relative angle of attack, an increase in relative angle of attack causes the inflection and interaction points to be shifted slightly downstream (Figs. 12b and 12c). In addition, the strength of the shock waves from both the bow shock and wing shock increases (Fig. 13).

The aerodynamic coefficients (including lift, drag, and pitching-moment coefficients of the three different EOS positions) are given in Table 4. In this table, the experimental data are also provided as references. The lift coefficient of the EOS vehicle decreases with increasing relative distance of the orbital vehicle. This is due to the increase in the gap area between the EOS and flat plate yielding higher flow velocity and lower static pressure on the lower surface; in turn, lift of the orbital stage decreases, and the lift coefficient increases and becomes a positive value, due to the increase in relative angle of attack. Increasing angle of attack of the orbital stage results in the gap area getting smaller downstream. Such a convergent gap will decelerate supersonic flow downstream, which causes an increase in static pressure on the lower surface and, in sequence, the lift increases. Concerning the drag coefficient, the main contribution is of the shock wave drag. The calculated drag coefficients do not significantly change due to the alterations of the relative distance and relative angle of attack. Comparing with the experimental results, the calculated lift coefficient provides very good agreement for the cases with zero relative angle of attack, with the error varying from 3 to 5%. But for the case with a positive relative angle of attack, the error of the computed lift coefficient increases to become about 10%, and the error of the drag is in the range of 5 to 7%. In the computation, increasing the relative distance and angle of attack of the orbital stage yields the reduction of negative pitching-moment coefficient. This is because the additional load obtained by the shock wave on the rear lower surface of the orbital stage moves to the wake region when the relative distance and angle of attack of the orbital stage increases, whereas in the experiment, the pitching-moment coefficients become more negative with increasing the relative distance and angle of attack of the orbital stage. This is caused by the present shock wave emanating from the leading edge of the flat plate on the lower surface producing the additional aft load of the EOS. The inflection point on the lower surface is located downstream of the moment reference point of the orbital stage ($x/l_{\mathrm{EOS}} = 0.65$), as shown in Fig. 14. As a result, a more negative pitching-moment coefficient is attained.

Furthermore, the effects of Mach number variation on the flowfield and aerodynamic characteristics are studied. Figure 15 shows the density distributions on the symmetry plane for Mach numbers of 4.0, 6.8, and 7.9 with the orbital stage positioned relative to the flat plate at $\Delta\alpha = 0.0$ deg and $h/l_{\mathrm{EOS}} = 0.150$. With increasing Mach number, the bow shock angle decreases, and hence the inflection point on the flat plate is shifted downstream. The areas of lower density become larger in the region of the base and the rear part of the

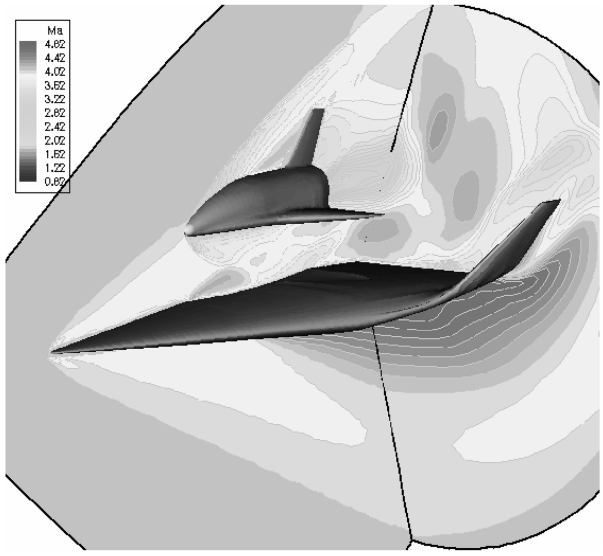

a) $h/l_{\mathrm{EOS}} = 0.225$, $\Delta\alpha = 0.0$ deg

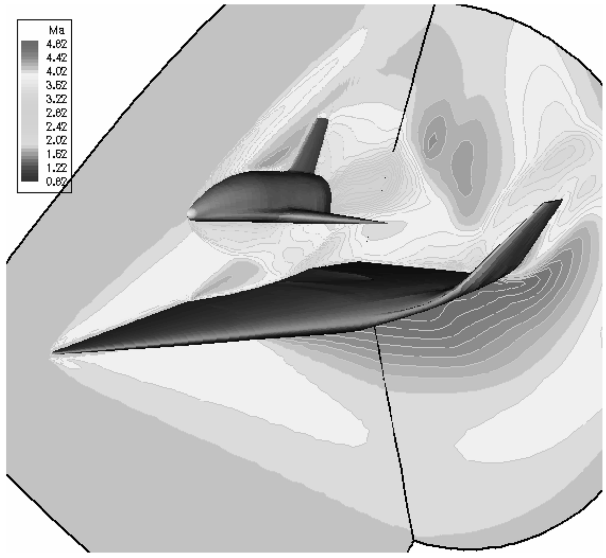

b) $h/l_{\mathrm{EOS}} = 0.225$, $\Delta\alpha = 5.0$ deg

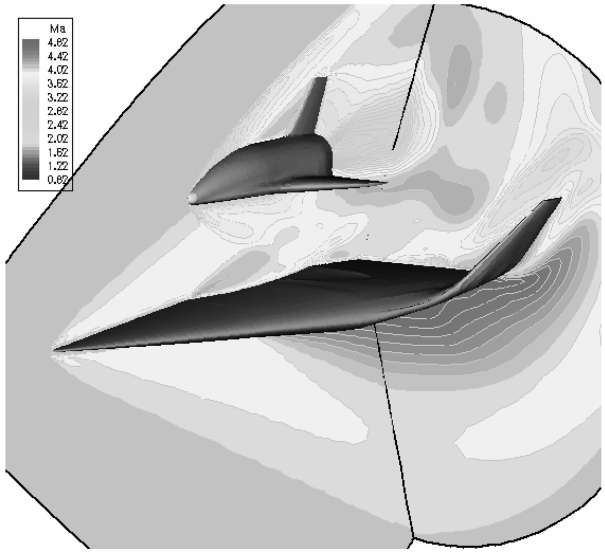

c) $h/l_{\mathrm{EOS}} = 0.325$, $\Delta\alpha = 0.0$ deg

Fig. 17 Effects of relative incidence and relative distance on flow behavior of EOS and ELAC stages at $M_\infty = 4.0$.

Table 6 Aerodynamic characteristics of EOS and ELAC for cases with different relative incidence and relative distance at $M_\infty = 4.0$

	$h/l_{\text{EOS}} = 0.225$, $\Delta\alpha = 0.0$			$h/l_{\text{EOS}} = 0.225$, $\Delta\alpha = 5.0$			$h/l_{\text{EOS}} = 0.325$, $\Delta\alpha = 0.0$		
	Comp	Exp	% diff	Comp	Exp	% diff	Comp	Exp	% diff
				EOS vehicle					
Lift coef. C_L	0.0292	0.0366	20.2%	0.1104	0.1311	15.8%	0.0225	0.0332	32.2%
Drag coef. C_D	0.0293	0.0337	13.1%	0.0368	0.0304	21.1%	0.0287	0.0317	9.5%
Pitching-moment coef. C_M	−0.0073	−0.0072	1.4%	−0.0259	−0.0082	215.9%	−0.0161	−0.0137	17.5%
				ELAC vehicle					
Lift coef. C_L	−0.0504	−0.0491	2.6%	−0.0628	−0.0623	0.8%	−0.0439	−0.0394	11.4%
Drag coef. C_D	0.0133	0.0164	18.9%	0.0131	0.0163	9.6%	0.0130	0.0164	20.7%
Pitching-moment coef. C_M	0.0077	0.0089	13.5%	0.0105	0.0105	0.0%	0.0057	0.0062	8.1%

lower surface of the EOS at the higher Mach number. Also, the band of higher density becomes bigger in the region of the shock waves. Table 5 shows aerodynamic coefficients of the EOS vehicle for the two different Mach numbers. By increasing the Mach number, the lift coefficient becomes more negative. This is due to the bow shock at higher Mach numbers producing lower pressures in the region below the orbital stage. As a result, the interaction between the orbital stage and the flat plate is more dangerous at higher Mach numbers. The drag is mainly caused by the shock wave. The drag coefficient decreases with increasing Mach numbers, as indicated by reduction of the peak static pressure on the flat plate (Fig. 16). In addition, the peak pressure distribution is shifted downstream at higher Mach numbers. By increasing the Mach number, the shock waves become more oblique; in turn, the strength of the shock wave becomes weaker and the drag decreases. Concerning the pitching moment, the magnitude of the pitching-moment coefficient decreases with increasing the Mach number. A decrease in the negative pitching moment is caused by a decrease in the aft aerodynamic loads on the lower surface of the orbital stage. This is indicated by the shock wave hitting the lower surface to be shifted downstream with increasing the Mach number.

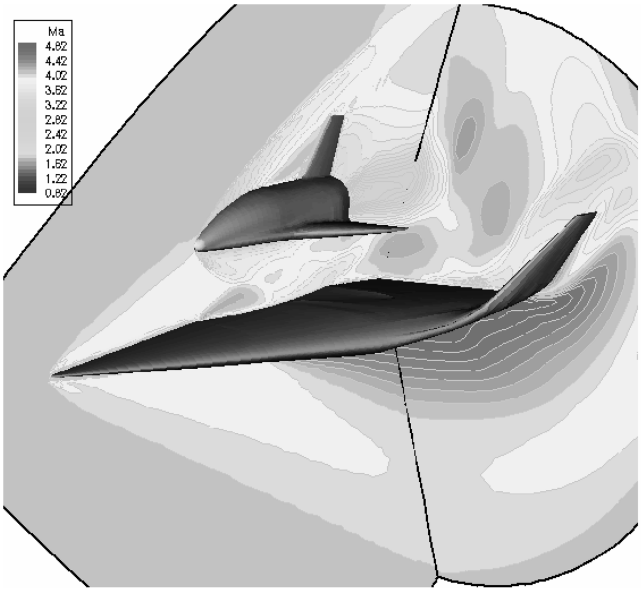

a) $h/l_{\text{EOS}} = 0.225$, $\Delta\alpha = 0.0$ deg, $\alpha = 0.0$ deg

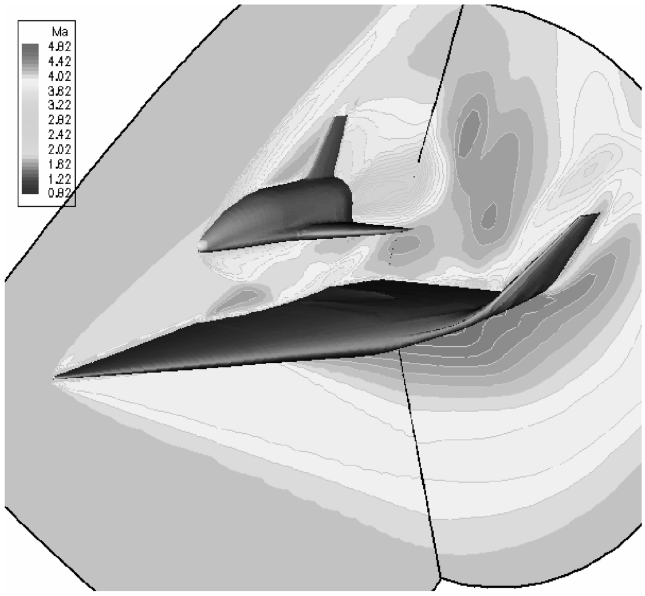

b) $h/l_{\text{EOS}} = 0.225$, $\Delta\alpha = 0.0$ deg, $\alpha = 3.0$ deg

Fig. 18 Effects of carrier-stage angle of attack on flow behavior of EOS and ELAC stages at $M_\infty = 4.0$.

C. Quasi-Steady Stage Separation: ELAC–EOS

The effects of relative incidence and relative distance on the flow behavior of the EOS and ELAC, which are computed based on finer grid at a freestream Mach number of 4.0, are shown by the Mach number contours in Fig. 17. With increasing the relative angle of attack, the bow shock wave of the ELAC moves further downstream, below the front part of EOS, and interacts with the lower bow shock of the EOS. Also, the impingement of the EOS bow shock wave is located further downstream, on the rear part of the upper surface of the ELAC stage. With the increase of the gap area, the interaction between the bow shock wave of the ELAC and the EOS lower bow shock wave occur at a location further downstream of the EOS nose. The lower bow shock wave itself passes through the flowfield at the gap and strikes on the rear part of the ELAC stage. In addition, the shock wave emanating from the curvature of the ELAC cavity moves to the rear part of the lower surface of the EOS.

Table 6 shows the aerodynamic coefficients of the EOS and ELAC stages for the two relative angles of attack and two relative distances. The increase of angle of attack of EOS provides an additional lift of this stage, but it amplifies the negative lift of the ELAC stage. Increasing the relative distance between the stages results in a reduced lift coefficient of the orbital stage and in a decrease of the negative lift of the ELAC stage. Concerning the drag coefficient, the computational results show a different tendency, compared with the experimental data for increasing relative angle of attack. The measured drag coefficient decreases, but the calculated one increases. The calculated drag coefficient is very sensitive to the location of interaction between the upper ELAC bow shock wave and the EOS bow shock wave. However, the increase of relative

Table 7 Comparison of aerodynamic characteristics of EOS and ELAC for cases with different angle of attack of carrier stage at $M_\infty = 4.0$

	EOS vehicle		ELAC vehicle	
	$\alpha = 0.0$	$\alpha = 3.0$	$\alpha = 0.0$	$\alpha = 3.0$
Lift coef. C_L	0.0292	0.0398	−0.0504	−0.0061
Drag coef. C_D	0.0293	0.0308	0.0133	0.0106
Pitching-moment coef. C_M	−0.0073	−0.0095	0.0077	0.0123

distance leads to a reduction of the drag coefficient of the EOS stage and a slight decrease of the ELAC drag. Furthermore, for all relative angles of attack $\Delta\alpha$, the orbital stage (EOS) provides a negative pitching-moment coefficient and the carrier stage (ELAC) presents a positive pitching moment. This means that with increasing $\Delta\alpha$, the nose-down magnitude of the pitching moment of EOS will increase, which has to be carefully addressed in the flight control system.

The effects of carrier-stage angle of attack on the flow behavior and aerodynamic characteristics of the EOS and ELAC are also examined. Two 3-D Mach contours for two different carrier-stage angles of attack (namely, $\Delta\alpha = 0.0\,\text{deg}$, $\alpha = 3.0\,\text{deg}$, and $M_\infty = 4.0$) are depicted in Fig. 18. An increase of the carrier-stage angle of attack results in the change of the ELAC bow shock line. Consequently, the supersonic flows behind the lower part of the ELAC bow shock decelerates, producing an increase in static pressure on the lower surface of the ELAC, whereas the flows on the front of the gap region undergo an acceleration and the surface pressure of the upper part of the ELAC decreases. The upper part of the ELAC bow shock moves up and interacts with the upper part of the EOS bow shock. As a consequence of the increase of flow velocity in front of the gap region, the supersonic velocity in the gap region increases, and hence both the orbital and carrier stages feel a suction flow. Thus, this affects the aerodynamic characteristics of the EOS and ELAC vehicles, as given in Table 7. Increasing the carrier-stage angle of attack provides higher additional lift for the carrier stage than with the EOS, and it gives a slight decrease in drag coefficient for both stages.

Concerning the pitching-moment coefficient of the ELAC–EOS configuration, the increase in angle of attack of the carrier stage provides more positive pitching-moment coefficient of the ELAC; oppositely, it produces a more negative pitching moment of the EOS. For the ELAC, the fore part of the lower surface undergoes higher aerodynamic load, owing to the increase in the strength of the shock wave, and the aft part experiences a lower aerodynamic load on account of the expansion wave and, consequently, more positive pitching moment to be attained. For the EOS, the increment of the negative pitching moment is caused by higher load of the EOS wing.

IV. Conclusions

Simulations of quasi-steady state of stage separation of a TSTO space transport system have been accomplished to investigate the influence of the changes of relative distance and angle of attack of the orbital stage as well as the effect of Mach number on aerodynamic flow behavior and characteristics. Two different configurations has been analyzed: namely, first, the carrier stage is idealized as a flat plate interfering with the orbital stage (EOS); second, the carrier stage refers to the complete geometry (ELAC) with the same orbital stage. The numerical grid parameters including grid smoothing and grid density are studied. They affect the improvement of the grid quality to be orthogonal, which provides sharper shock waves. The simulations for the two configurations exhibit good-to-excellent agreement with the experimental reference values. For the flat-plate–EOS configuration, the calculated lift coefficients give very good agreement for the cases with zero relative angle of attack, compared with the corresponding experimental results. But for the case with a positive relative angle of attack, the error of the computed lift coefficient increases, whereas the computed drag gives reasonable agreement compared with the corresponding experimental data. In addition, the large discrepancy of pitching-moment coefficient between the computation and experiment is caused by the lack of simulating of the shock wave emanating from the leading edge of the flat plate. For the ELAC–EOS configuration, the relative distance and relative angle of attack provide effects on the shock wave similar to those with the flat-plate–EOS configuration. However, the two different carrier stages of the vehicle system show opposite effects on the lift coefficient of the orbital stage. In addition, the calculated aerodynamic coefficients shows good agreement compared with the corresponding experimental data, except the pitching-moment coefficient of the EOS configuration at higher angle of attack.

The numerical solution based on the Euler approach, which assumes the flowfield to be inviscid, used in this investigation is sufficient to obtain highly accurate results. This is because the separation problem of two-stage-to-orbit takes place at hypersonic speed and the flow has a higher Reynolds number. Under these conditions, boundary layers on the vehicle surfaces are limited and so may be ignored. The Reynolds-averaged Navier–Stokes approach may improve the computation results, especially for simulating more accurate flow in the gap region when shock-wave/boundary-layer interactions occur or for a case with a very limited relative distance between both stages. In such cases, the effect of the boundary layer will be significant, but it will require 5 times the grid number for doing the simulation.

The simulation of the stage separation by considering time-dependent flow will be presented in part 2. The unsteady-flow solution is obtained by solving Euler equations using a dual-time-stepping methodology. This method employs pseudotime to redefine the unsteady-flow problem into a steady-flow problem, with the physical time derivative included in the discretized equations.

Acknowledgment

The subject of this paper is part of the research undertaken in the Collaborative Research Center 255 program, "Transatmospheric Flight Systems—Fundamentals of Aerothermodynamics, Propulsions and Flight Mechanics" of Deutsche Forschungsgemeinschaft (DFG) at the Technische Universität München.

References

[1] Russo, G., "Next Generation Space Transportation System," *Aerotecnica, Missili e Spazio*, Vol. 81, No. 2, 2002, pp. 65–72.

[2] Kuczera, H., Hauck, H., Krammer, P., and Sacher, P. W., "The German Hypersonic Technology Programme," International Astronautical Federation Paper 93-V.4.629, 1993.

[3] Maita, M., and Kubota, H., "Japanese Space Plan/RLV Program," *8th AIAA International Aerospace Planes and Hypersonic System and Technologies Conference*, AIAA, Reston, VA, 1998.

[4] "Space Transportation: Challenges Facing NASA's Space Launch Initiative," General Accounting Office Rept. GAO-02-1020, Washington, D.C., Sept. 2002.

[5] Yanagihara, M., and Munenaga, T., "High-Speed Flight Demonstration Project," *24th International Congress of the Aeronautical Sciences*, General Accounting Office, Washington, D.C., 2004, pp. 711.1–711.10.

[6] Laschka, B., and Breitsamter, C., "Transatmosphärische Flugsysteme–Grundlagen der Aerothermodynamik, Antriebe und Flugmechanik," *Sonderforschungsbereich 255*, Technische Univ. München, Garching, Germany, June 2001, pp. 23–94.

[7] Decker, K., *Aerodynamik Eines Zweistufigen Raumtransportsystems Beim Wiedereintritt und Während der Separation*, Ph.D. Dissertation, Technische Univ. München, Munich, 2003.

[8] Kharitonov, A., Brodetsky, M., Vasenyov, L., Adamov, L., Breitsamter, C., and Heller, M., "Investigation of Aerodynamic Characteristic of the Models of a Two-Stage Aerospace System During Separation," Inst. of Theoretical and Applied Mechanics, Novosibirsk, Russia, and Technische Univ. München, Munich, 2000.

[9] *Meshing Tutorial Manual*, ICEM CFD Engineering, Berkeley, CA, 2002.

[10] Thompson, J. F., Soni, B. K., and Weatherill, N. P., *Handbook of Grid Generation*, CRC Press, Boca Raton, FL, 1999.

[11] Cvrlje, T., Breitsamter, C., Weishäupl, C., and Laschka, B., "Euler and Navier-Stokes Simulations of Two-Stage Hypersonic Vehicle Longitudinal Motions," *Journal of Spacecraft and Rockets*, Vol. 37, No. 2, Mar.–Apr. 2000, pp. 242–251.

[12] Radespiel, R., and Kroll, N., "Accurate Flux Vector Splitting for Shock and Shear Layers," *Journal of Computational Physics*, Vol. 121, No. 1, Oct. 1995, pp. 66–78. doi:10.1006/jcph.1995.1179

[13] Liou, M. S., and Steffen, Ch., "A New Flux Splitting Scheme," *Journal of Computational Physics*, Vol. 107, No. 1, July 1993, pp. 23–39. doi:10.1006/jcph.1993.1122

[14] Van Leer, B., "Towards the Ultimate Conservative Difference Scheme 5: A Second Order Sequel to Gudonov's Method," *Journal of Computational Physics*, Vol. 32, No. 1, July 1979, pp. 101–136. doi:10.1016/0021-9991(79)90145-1

R. Cummings
Associate Editor